STAR FORMATION ACTIVITY IN A YOUNG GALAXY CLUSTER AT $Z = 0.866$

T. F. Laganá[1], M. P. Ulmer[2], L. P. Martins[1], AND E. da Cunha[3]

[1] NAT, Universidade Cruzeiro do Sul, Rua Galvão Bueno, 868, CEP: 01506-000, São Paulo/SP, Brazil
[2] Department of Physics and Astronomy and CIERA, Northwestern University, 2145 Sheridan Road, Evanston IL 60208-3112, USA
[3] Center for Astrophysics and Supercomputing, Swinburne University of Technology, Hawthorn VIC 3122, Australia

ABSTRACT

The galaxy cluster RX J1257+4738 at $z = 0.866$ is one of the highest redshift clusters with a richness of multi-wavelength data, and is thus a good target to study the star formation–density relation at early epochs. Using a sample of spectroscopically confirmed cluster members, we derive the star-formation rates (SFRs) of our galaxies using two methods: (1) the relation between SFR and total infrared luminosity extrapolated from the observed *Spitzer* Multiband Imaging Photometer for *Spitzer* 24 μm imaging data; and (2) spectral energy distribution fitting using the MAGPHYS code, including eight different bands. We show that, for this cluster, the SFR–density relation is very weak and seems to be dominated by the two central galaxies and the SFR presents a mild dependence on stellar mass, with more massive galaxies having higher SFR. However, the specific SFR (SSFR) decreases with stellar mass, meaning that more massive galaxies are forming fewer stars per unit of mass, and thus suggesting that the increase in star-forming members is driven by cluster assembly and infall. If the environment is somehow driving the star formation, one would expect a relation between the SSFR and the cluster centric distance, but that is not the case. A possible scenario to explain this lack of correlation is the contamination by infalling galaxies in the inner part of the cluster, which may be on their initial pass through the cluster center. As these galaxies have higher SFRs for their stellar mass, they enhance the mean SSFR in the center of the cluster.

Key words: galaxies: clusters: individual (RX J1257+4738) – galaxies: clusters: intracluster medium – galaxies: high-redshift – galaxies: interactions – galaxies: photometry – galaxies: star formation

1. INTRODUCTION

It has been known since the pioneering work of Dressler (1980) that higher density environments in the local universe host more elliptical and S0 galaxies, meaning that they are dominated by evolved galaxy populations. This fact illustrates the impact of the large-scale environment on galaxy properties. Since there is a strong correlation between the Hubble type and the star-formation rate (SFR; Kennicutt 1998), a correlation between the SFR and local galaxy density is expected and has been observed in recent studies (e.g., Gómez et al. 2003; Balogh et al. 2004; Blanton & Moustakas 2009). That is, the relative number of star-forming galaxies and quiescent galaxies varies strongly with local density, showing that red, quiescent, early-type galaxies represent a large proportion of the population in higher density regions at low redshift, such as the core of galaxy groups and clusters, while blue, star-forming, late-type galaxies are predominant in lower density regions.

Extensive observational efforts at low redshift have yielded a paradigm for galaxy environmental dependencies, such that the densest regions at $z \simeq 0$ harbour massive (Kauffmann et al. 2004), red (Balogh et al. 2004), early-type passive galaxies (Dressler 1980). At $z \simeq 0$, several studies have found the mean SFRs of galaxies to be lower at higher densities such as in groups and clusters (e.g., Gómez et al. 2003; Kauffmann et al. 2004). However, while it is well established that higher redshift clusters contain increased star formation activity compared to their local counterparts (e.g., Butcher & Oemler 1978; Bai et al. 2007; Saintonge et al. 2008; Patel et al. 2011; Webb et al. 2013), which is in line with the rapid decline of cosmic SFR since $z \simeq 1$ (Lilly et al. 1996; Madau et al. 1996; Le Floc'h et al. 2005; Hopkins & Beacom 2006), there has not yet been a consensus on the SFR–density relation at this epoch. For example, using luminosity-limited samples, Elbaz et al. (2007) and Cooper et al. (2008) find

that, at $z \simeq 1$, the SFR–density relation reverses, such that galaxies in higher density environments have enhanced SFRs. However, for a stellar-mass-limited sample at $z \simeq 0.8$, Patel et al. (2009) find that the SFR declines at higher densities, much like at $z \simeq 0$. The difference between these studies could be the result of different sample selections probing very different environment densities (Patel et al. 2009, 2011). Nevertheless, this shows that more work is needed to understand how the effect of environment on galaxy evolution evolves with redshift.

The cosmic time around redshift $z \simeq 1$ is crucial to understand cluster and galaxy evolution because it is most likely the epoch of the first mature galaxy clusters (e.g., Kravtsov & Borgani 2012). This makes the redshift range between 0.8 and 1.0 particularly interesting for comparing the star-formation histories of galaxies in clusters and in the field, as well as studying the relationship between infalling galaxies and gas heating. The direction of the SFR–density relation at $z \simeq 1$ has implications for the role of the various physical processes that operate in different environments regulating star formation (SF) and the evolution of galaxies. It appears that the physical mechanisms that relate galaxies with their environment are more complex than initially thought, and cannot be reduced solely to ram pressure stripping from the intracluster medium (ICM) of massive galaxy clusters (see the discussion in Balogh et al. 2004). If, for example, a direct correlation between the SFR and local density is observed at $z \simeq 1$, that would imply that the physical processes leading to the quenching of SF in high-density environments produce fewer red, non-star-forming galaxies.

A widely used method to follow the build-up of galaxies through time is to look into the evolution of their optical colors. Observed galaxy populations show a bimodal distribution in color–magnitude diagrams, which separate red, passively evolving galaxies from the blue, actively star-forming galaxies. Recent studies have demonstrated that this bimodality was already in

place at $z \simeq 1$, with red galaxies preferentially located in the densest regions (e.g., Cooper et al. 2006; Cucciati et al. 2006). However, the optical color of a galaxy is not straightforwardly linked with its instantaneous SFR, since it is also affected by dust content, and the past SF history of the galaxy.

A recent strategy to overcome these difficulties and understand the SFR–density relation is to directly measure the instantaneous SFR as a function of redshift and environment using multi-wavelength diagnostics beyond solely optical colors. In a previous work, Ulmer et al. (2009) presented a multi-wavelength analysis of the cluster RX J1257+4738 using optical, near-, and far-infrared data to determine its dynamical state, and to gain insights into its galaxy population properties. However, this study is incomplete, because the *Spitzer* data were not sufficiently well calibrated to be analyzed at the time of that study, which could potentially affect the measurements of the SFR and stellar mass of the cluster galaxies.

The *Spitzer* archive now contains reliably calibrated photometric data for this cluster in all observed bands, which allows us to carry out a detailed analysis of the stellar mass content and SF activity of this distant X-ray emitting young cluster of galaxies. In this paper, we use the deepest existing mid-infrared survey at 24 μm, with some of the largest spectroscopic completeness to analyze the relationship between the SFR and the specific SFR (SSFR) as a function of projected cluster centric distance (as an indication of the density) in a galaxy cluster at $z = 0.866$: RX J1257+4738.

In principle, this approach might seem similar to that of Pintos-Castro et al. (2013; hereafter PC13), who also performed a multi-wavelength analysis of the galaxies in this cluster. Our current study differs from PC13 in two crucial aspects. First, our spectroscopic observations allow us to establish cluster membership of the galaxies more robustly than PC13, who used photometric redshifts in their analysis. Second, we find that in PC13 there was a misconception that there were no Multiband Imaging Photometer for *Spitzer* (MIPS) sources associated with the western cluster members. We discuss the properties of these "missing sources," and explain why PC13 were not able to associate these MIPS sources with cluster members. Since we successfully identified MIPS sources near the cluster center that are clusters members, we provide a different interpretation from PC13 of the observations of RX J1257 by updating the work of Ulmer et al. (2009) with robust constraints of the SFR and SSFR of the galaxies enabled by the *Spitzer* data.

The paper is organized as follows: in Section 2 we present the spectroscopic and imaging data used in this paper, in Section 3 we describe the methods to determine the physical properties of the galaxies (SFRs and stellar masses). We present our results in Section 4, the discussion in Section 5, and present our conclusions in Section 6. Throughout this paper, we assume a concordant ΛCDM cosmology with $\Omega_m = 0.27$, $\Omega_\Lambda = 0.7$, $H_0 = 71$ km s^{-1} Mpc^{-1}, from which we compute the angular scale as 7.72 kpc arcsec^{-1}, a luminosity distance (D_L) = 5544.7 Mpc, and an angular distance (D_A) = 1592.4 Mpc. This cluster is centered at R.A. = $12^h 57^m 12\overset{s}{.}2$, decl. = $+47^o 38' 06\overset{''}{.}5$ (J2000) and the virial radius, based on the temperature of the ICM and using the formula from Hilton et al. (2007), is $R_{vir} = 1.05$ Mpc (Ulmer et al. 2009; Pintos-Castro et al. 2013). Ulmer et al. (2009) inferred an X-ray mass of $(1-5) \times 10^{14} M_\odot$ and based on a velocity dispersion of 600 km s^{-1}; however, these authors obtained an independent mass estimate of $6.1 \times 10^{14} M_\odot$. All magnitudes are

quoted in the AB system and confidence intervals correspond to the 68% confidence level unless otherwise stated.

2. DATA ANALYSIS

2.1. Spitzer Imaging

We use Infrared Array Camera (IRAC; Fazio et al. 2004) and MIPS (Rieke et al. 2004) data downloaded from the *Spitzer* Heritage Archive[4] (SHA). There were 20 IRAC frames with 100 s integration time per frame, centered at each of the channels 3.6, 4.5, 5.8, and 8 μm, and 30 s integration time MIPS frames, centered at 24 μm, resulting in a total of 9050 s exposure time. The calibrated mosaic images from the standard *Spitzer* pipeline showed satisfactory removal of instrumental artifacts and were sufficiently clean for the IRAC data analysis. However, the MIPS 24 μm pipeline mosaic exhibited artifacts and gradients which were significantly reduced through a zodiacal light subtraction, a self-calibrating flat, and an improved overlap correction algorithm. We converted the original flux values from MJy/sr to μJy, taking into account the pixel size to which these images were rebinned and using the conversion factor provided in the IRAC Handbook.

One of the major differences between the data used in this work and in PC13 is regarding the MIPS 24 μm fluxes. It appears that the data used by PC13 were not the latest data set processed through the *Spitzer* pipeline, which can be found in the SHA. We note that the faintest source in our catalog has a MIPS 24 μm flux of 20 μJy (i.e., $m = 20.6$), which is fainter than the completeness limit of $m = 19.2$ quoted by PC13. The MIPS flux density is measured using SHA with a default aperture of diameter 14.7 arcsec and checked using flux integration package (Aper referenced by the SHA) by hand to confirm if SHA returns the correct fluxes of our targeted galaxies. In comparison, PC13 used SExtractor and auto-flux except augmented by the APEX package for objects missed by SExtractor. This will lead to different SFR results, as shown in Section 4.

For the few blended sources (see notes on the sources in Appendix A), we used the *aper.pro* IDL procedure[5] based on the IRAF tool DAOPHOT (Stetson 1987, 1992). For uncertainties in these cases, we obtained the uncertainty files provided by the SHA, and cross-checked our derived values by comparing the results we derived for unblended sources, and the results are consistent.

2.2. Gemini Spectroscopy

We acquired three Gemini North GMOS observations (GN-2005A-Q-9, GN-2006A-Q-4, and GN-2006B-Q-38), for which the imaging process and data reduction is described in a previous paper by Ulmer et al. (2009). We took advantage of the pre-imaging observation to acquire two deep optical images of this cluster in the i' and z' bands. We obtained images in the i' band under photometric conditions. Images in the z' band were observed under non-photometric conditions.

To measure redshifts in our $z \simeq 0.9$ galaxy cluster, we required spectroscopic observations of galaxies as faint as $i' \simeq 23$. We obtained spectra of 45 galaxies with magnitudes between $i' = 20$ and 22.6 with exposure times varying between 3 and 4 hr (within this configuration we reach S/N = 2.5 per resolution unit, that is $\sim$2.5 pixels or 7.5 Å). Individual redshifts were determined through cross-correlating the observed spectra with a set of

---

Table 1
Properties of the Cluster Galaxies

Source Code	Redshift	R.A. (J2000)	Decl. (J2000)	$SFR_{MAGPHYS}$ ($M_\odot$ yr^{-1})	$M_{star\,MAGPHYS}$ ($10^{11}M_\odot$)	flux$_{MIPS}$ (μ Jy)	SFR_{MIPS} ($M_\odot$ yr^{-1})	SSFR (10^{-10} yr^{-1})	Projected Dist. (Mpc)
1	0.874	194.2342	47.6325	$9.3^{+2.6}_{-2.9}$	$1.15^{+0.39}_{-0.47}$	98.8 ± 10.0	8.5 ± 0.9	0.86 ± 0.27	1.26
2	0.865	194.2500	47.6371	$6.4^{+1.1}_{-1.1}$	$0.98^{+0.16}_{-0.15}$	218.7 ± 6.9	21.4 ± 0.7	3.26 ± 0.48	0.97
3	0.871	194.2503	47.6183	$5.2^{+2.0}_{-1.2}$	$0.15^{+0.02}_{-0.03}$	64.8 ± 8.3	5.0 ± 0.6	3.11 ± 0.96	1.05
4	0.853	194.2556	47.6026	$4.6^{+1.6}_{-1.4}$	$1.70^{+0.29}_{-0.25}$	151.0 ± 10.1	13.7 ± 0.9	1.41 ± 0.39	0.96
5	0.853	194.2571	47.5995	$11.9^{+1.5}_{-1.6}$	$1.07^{+0.22}_{-0.28}$	383.2 ± 10.3	39.2 ± 1.1	6.30 ± 1.25	1.22
6	0.863	194.2670	47.6262	$10.0^{+1.7}_{-1.7}$	$0.85^{+0.11}_{-0.15}$	56.2 ± 6.9	4.2 ± 0.5	0.76 ± 0.20	1.27
7	0.873	194.2797	47.6179	$7.6^{+1.6}_{-2.0}$	$0.07^{+0.02}_{-0.02}$	63.8 ± 7.0	4.9 ± 0.5	3.66 ± 0.95	0.60
8	0.858	194.2830	47.6190	$5.8^{+1.3}_{-1.3}$	$2.04^{+0.30}_{-0.20}$	48.4 ± 7.0	3.5 ± 0.5	0.27 ± 0.07	0.54
9	0.862	194.2950	47.6325	$47.5^{+1.4}_{-1.4}$	$2.51^{+0.52}_{-0.31}$	20.7 ± 6.9	1.4 ± 0.5	0.09 ± 0.04	0.13
10	0.864	194.2950	47.6342	$111.4^{+2.3}_{-2.1}$	$6.17^{+0.28}_{-0.29}$	1642.1 ± 6.9	208.7 ± 0.9	13.11 ± 2.01	0.12
11	0.856	194.2970	47.6187	$16.1^{+1.4}_{-1.4}$	$2.45^{+0.37}_{-0.30}$	109.8 ± 7.0	9.9 ± 0.6	0.55 ± 0.11	0.43
12	0.865	194.2992	47.5864	$33.7^{+1.6}_{-1.7}$	$1.23^{+0.42}_{-0.51}$	591.8 ± 10.0	65.9 ± 1.1	5.31 ± 0.91	1.32
13	0.865	194.3040	47.6360	…	…	21.0 ± 6.9	1.4 ± 0.5	0.07 ± 0.03	0.07
14	0.853	194.3099	47.6393	$8.6^{+2.4}_{-2.5}$	$1.00^{+0.38}_{-0.48}$	259.7 ± 7.1	25.0 ± 0.7	7.19 ± 1.14	0.22
15	0.860	194.3142	47.6571	$78.9^{+1.5}_{-1.0}$	$0.11^{+0.05}_{-0.01}$	112.0 ± 7.6	10.0 ± 0.7	4.07 ± 0.96	0.69
16	0.860	194.3441	47.6341	$12.9^{+1.8}_{-2.9}$	$0.31^{+0.07}_{-0.09}$	92.4 ± 9.5	7.3 ± 0.7	2.22 ± 0.64	0.80
17	0.859	194.3470	47.6140	$14.2^{+2.3}_{-1.9}$	$1.29^{+0.19}_{-0.22}$	28.1 ± 6.9	1.9 ± 0.5	0.22 ± 0.08	1.02
18	0.860	194.3592	47.6244	$9.9^{+2.2}_{-2.11}$	$0.72^{+0.30}_{-0.42}$	264.2 ± 13.5	26.0 ± 1.3	6.26 ± 1.70	1.11

templates of several different galaxy types. We used the Ca II H&K lines (3934, 3964 Å) and [O II] emission line (3727 Å) as the main ones for the redshift determination. From the total of 45 spectra we measured, we consider cluster members to be all galaxies with redshift between 0.85 and 0.87 which corresponds to a velocity dispersion of $\sim$2500 km s^{-1} relative to the cluster redshift (the same limits as PC13), with uncertainties on the velocity determinations of less than $\sim$200 km s^{-1}.

We note that, apart from the redshifts, very little additional information on the physical properties of the galaxies can be obtained from these spectra. The flux calibration is very uncertain and the signal-to-noise ratio (S/N) is very low, which makes it impossible to extract meaningful information on the stellar population of the galaxies from these spectra.

2.3. Near-infrared Imaging

We also obtained near-infrared data (J and K_s bands), which allow us to fill the gap between the Gemini i' and z' bands and the *Spitzer* IRAC and MIPS mid-infrared bands. We obtained a J-band Subaru MOIRCS image with 40 minute exposure in 2007. We also observed a subfield of the RX J1257 in the K_s band for two hours. This provided a complete catalog up to $K_s \simeq 22$. Details about these observations can be found in Ulmer et al. (2009).

2.4. Cluster Galaxies Sample

With the aim of building a multi-wavelength catalog that includes all detected sources, MIPS sources were matched with the near-IR observation catalog using a 3″ matching distance, which is half of the point-spread function (PSF) FWHM at 24 μm. Overall, 78% of objects with $i' < 23$ and in the good spectroscopic redshift range with MIPS coverage are matched to a MIPS source. In cases where multiple objects in the i band could be matched with the same MIPS source, the closest object was assigned as the match. Of all the objects assigned to a MIPS counterpart, only two were assigned to the closest of

multiple candidates. The result is a sample of 18 galaxies spectroscopically confirmed as cluster members. The positions and spectroscopic redshifts of these galaxies are presented in Table 1. We note that with our final sample of only 18 objects it is not possible to assume a rigorous completeness limit by searching for the turn over in the number counts versus flux.

3. SFRs AND STELLAR MASSES

In order to investigate the SF properties of our cluster galaxies, in this section we derive the SFRs of our cluster galaxies using two different methods: by fitting the full spectral energy distributions (SEDs) of our galaxies (Section 3.1), and by using the observed 24 μm emission to determine the total infrared luminosity, and converting that to an SFR (Section 3.2; this is a commonly used method when only infrared observations are available). To compute the SSFR, which is defined as the SFR/$M_\star$, we adopt the stellar masses $M_\star$ derived from SED fitting for both SFR determinations.

3.1. Determination Using the MAGPHYS Code

We fit the full observed SEDs of our galaxies using the MAGPHYS code (da Cunha et al. 2008; www.iap.fr/magphys). MAGPHYS interprets the full ultraviolet-to-infrared SED of galaxies in terms of several physical parameters related to the stellar content, SF activity, and dust content of galaxies using a Bayesian fitting method. The stellar population is modeled using the Bruzual & Charlot (2003) models, assuming a Chabrier (2003) initial mass function (IMF). The dust attenuation is modeled using the two-component model of Charlot & Fall (2000), which includes the attenuation of starlight by dust in stellar birth clouds and in the diffuse interstellar medium (ISM). The energy absorbed by dust in these regions is then re-radiated in the mid- to far-infrared range via an energy balance argument, and using dust emission templates to account for different components: poly cyclic aromatic hydrocarbons (PAHs), hot dust emitting in the

mid-infrared, and warm and cold dust in thermal equilibrium (more details in da Cunha et al. 2008).

We use the i', J, K_s, IRAC1, IRAC2, IRAC3, IRAC4, and MIPS 24 μm bands as inputs for MAGPHYS. We exclude the z' band because this band was observed under non-photometric conditions, and therefore the resulting fluxes are too uncertain. We present the resulting SED fits for each individual galaxy in Appendix C, and the the SFR and stellar masses constrained through this method in Table 1. Error bars from MAGPHYS are the 16th–84th percentile of the likelihood distribution of SFR resulting from the MAGPHYS SED fit.

3.2. Determination Using the Spitzer 24 μm Flux

In order to convert the 24 μm luminosity into a total infrared luminosity, we use the technique described in Chary & Elbaz (2001) and Elbaz et al. (2007), which is based on the observed correlation between the mid and far-infrared luminosity of local galaxies. A library of 105 template SEDs was built to reproduce those correlations including the tight correlation between the rest-frame $\sim$13 μm luminosity with L_{IR}, probed by the observed 24 μm passband for galaxies at $z \simeq 0.9$. For each cluster galaxy, we compute the rest-frame luminosity at 24 μm/$(1 + z)$ and compare it to the luminosity at that wavelength for each one of the 105 template SEDs, which allows us to identify the template with the closest luminosity. We then use this template, normalized to the observed luminosity of the galaxy at 24 μm/$(1 + z)$, to derive L_{IR} for that specific galaxy. To do so, we use the Kennicutt (1998) relation: $SFR_{IR}[M_\odot\ yr^{-1}] = 1.72 \times 10^{-10} L_{IR} [L_\odot]$.

We note that different IMFs lead to systematically different SFR derivations. The MAGPHYS SFR determination, described in the previous section, uses a Chabrier IMF, while the Kennicutt (1998) relation assumes a Salpeter IMF (Salpeter 1955). Thus, in order to make these two different determinations comparable, we rescale the SFR computed from *Spitzer* observations, using SFR [Salpeter] = 1.7×SFR[Chabrier] (e.g., Genzel et al. 2010). The resulting SFR and SSFR for each galaxy obtained using this method are also presented in Table 1.

4. RESULTS

4.1. Comparison of Different SFR Estimates

In this section, we compare the SFRs of our cluster galaxies obtained using the two methods described in the previous section.

We note that the MIPS-based and MAGPHYS estimates of the SFR are based on fundamentally different assumptions. The MIPS 24 μm flux traces the rest-frame mid-infrared (around 13 μm) of our cluster galaxies, which is dominated by a combination of hot dust and PAHs emission features, both heated by ultraviolet radiation emitted by young stars (i.e., ongoing SF). However, there are caveats in using this wavelength regime to constrain the SFR, specifically the fact that PAH emission depends strongly on metallicity, and that these dust components can also be heated by evolved stellar populations unrelated to current SF (Calzetti et al. 2010). The MIPS-based SFR estimates also suffer from the uncertainty in extrapolating from the rest-frame mid-infrared to the total infrared emission, which assumes that galaxy infrared SEDs do not vary significantly out to $z \simeq 1$.

The MAGPHYS modeling, on the other hand, interprets the full ultraviolet-to-infrared SED of galaxies in a self-consistent way, taking into account dust heating by young stars mostly associated
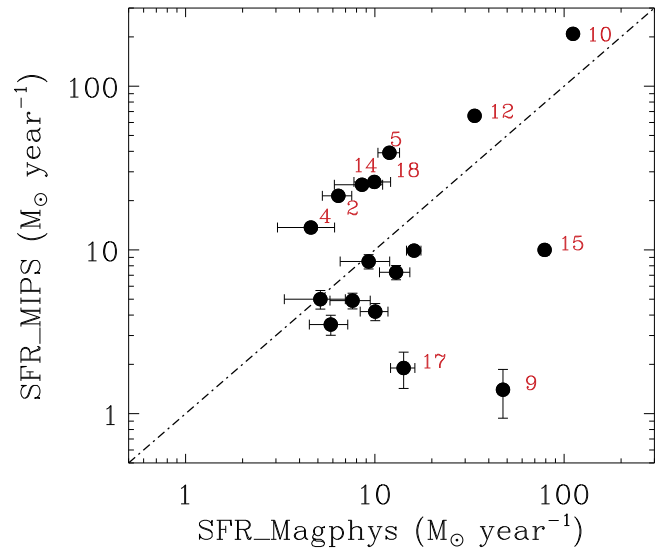

Figure 1. Comparison of the SFR values computed from the total IR luminosity extrapolated using the MIPS flux (Section 3.2) and the MAGPHYS code output (Section 3.1). In red we label the IDs of the sources with the largest differences between the two SFR estimates. The dashed line is the identity line.

with stellar birth clouds, and also heating by older stellar populations in the diffuse ISM. The extrapolation of the dust SEDs to wavelengths longer than 24 μm is done using a physically motivated energy balance technique and assuming a large variety of dust emission properties (such as temperatures, PAH fractions, etc.). In some cases, the presence of an active galactic nucleus (AGN) may also provide additional mid-infrared emission (from the heating of the dusty torus) which can contaminate the SFR estimates if not taken into account. This affects both the MIPS-based and MAGPHYS estimates of the SFR. Our SEDs (see Figures 7–8) point to little or no AGN contamination when compared to Figure 1 from Donley et al. (2012). Also, when taking the IRAC fluxes of these galaxies and putting them in an AGN mid-IR diagnostic plot (e.g., Stern et al. 2005; Lacy et al. 2007; Donley et al. 2012, but based on Figure 4 from the later reference), none of them lie in the current AGN selection regions.

In Figure 1, we show the comparison between the SFR derived from MIPS observation and using the MAGPHYS code. Galaxies with discrepant SFR values between the methods are identified in this figure using the source codes from Table 1. The SFR obtained from MIPS is significantly lower than the one obtained from MAGPHYS for galaxies identified as 9, 15, and 17. The reason they fall so far below the locus of the other galaxies may come from the different inferred total infrared luminosities. For these three galaxies, the L_{IR} derived from MAGPHYS is about one order of magnitude higher than the one computed using the MIPS flux, which could be due to the energy balance based on the stellar population modeling implying much higher dust luminosities than the dust SEDs Chary & Elbaz (2001) templates.

We can also speculate that this could be a metallicity effect such that PAHs can be weak (as shown by the MAGPHYS fits in Figures 7–8) or even absent in low-metallicity, star-forming galaxies (Engelbracht et al. 2005; Madden et al. 2006), or due to PAH destruction (e.g., Giard et al. 1994).

On the other hand, for many galaxies (identified as 2, 4, 5, 10, 12, 14, and 18) the opposite behavior is seen, where the SFR from MIPS is higher than the one obtained from MAGPHYS. One
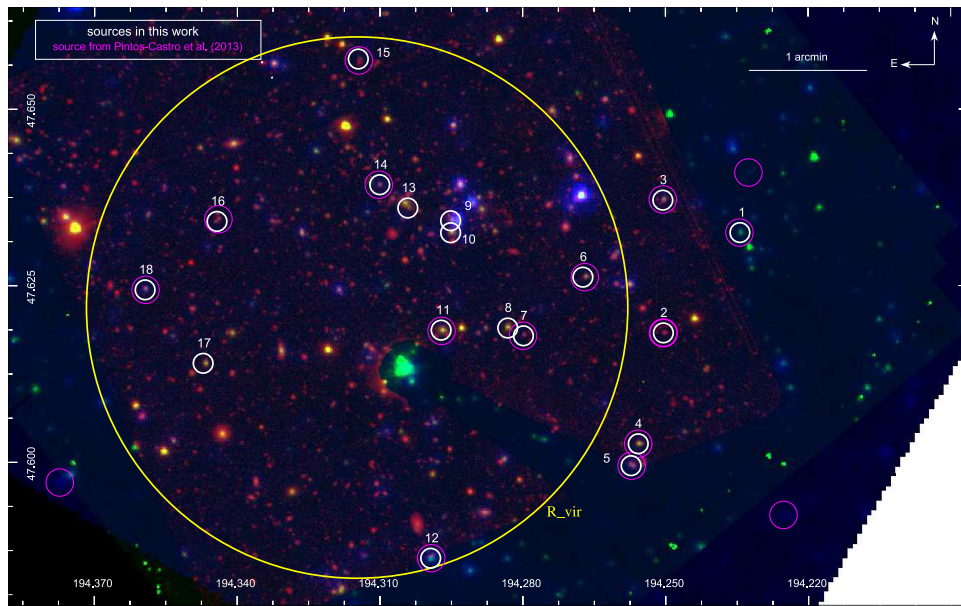
Figure 2. Color image of our cluster based on Gemini i' band image (R), *Spitzer* IRAC1 (G), and *Spitzer* MIPS 24 μm (B). White circles represent the galaxies within the cluster redshift range used in this work, and the large yellow circle corresponds to the virial radius of 1.05 Mpc. The magenta circles represent the galaxies at the cluster redshift range in Pintos-Castro et al. (2013). We have 11 out of 18 galaxies in common.

possible explanation is that these are galaxies in crowded regions, and most of them have at least one very close companion, whose MIPS flux might be contaminating the SFR determination (which is the case for galaxies identified as 2, 10, 12, 14, and 18). This explanation cannot be applied for two of these galaxies, identified as 4 and 5, however. Another equally likely explanation could be again related to the uncertainties on the relation of the $L_{\rm IR}$ with the SFR, but comparing the inferred total infrared luminosities, for galaxy identified as 4, the $L_{\rm IR}$ obtained from MAGPHYS is about 2 times higher than the $L_{\rm IR}$ derived from MIPS flux and for galaxy identified as 5, the $L_{\rm IR}$ computed with these two different methods agree. Then, the difference in SFR is probably due to different assumptions about dust heating. The IR method assumes that all of the dust emission is heated by current SF (i.e., young stars), but MAGPHYS allows for some of the dust emission to be heated by older stellar populations; therefore this allows for lower SFR.

4.2. Dependence of SFRs on Environment and Stellar Mass

In this section, we investigate in detail how the SF activity of our cluster galaxies depends on their environment by looking at their position within the cluster. In Figure 2, we present the spatial distribution of the galaxies used in this work and a comparison with the ones used in PC13. We note that PC13 considered three galaxies with no MIPS detection: R.A. = 194.2251, decl. = 47.5925; R.A. = 194.2324, decl. = 47.641; and R.A. = 194.3771, decl. = 47.5971 (the open magenta circles with no corresponding white circle in Figure 2), and they missed five galaxies in the innermost part of the cluster (inside $r_{\rm vir}$). Out of these, two were not identified by PC13 because they are a little more than 1 mag below their completeness limit (objects 9 and 13 in Table 1). Object 10, however, was possibly rejected by PC13 not because it is too faint, but because they associated its flux to a line of sight, non-cluster member. Other objects present in our sample that cannot be found in PC13 are objects 8 and 17. Object 8 (mag 19.6) is just below the PC13 completeness limit and object 17 (mag 20.2) is well below. Thus, only object 10 was not picked up by PC13

either because of image artifacts or because they attributed the MIPS flux to another galaxy. The different completeness limit suggests that the data used by PC13 was not the latest data set processed through the *Spitzer* pipeline, as mentioned before. Despite that, we still have 11 sources in common with their work.

For the 11 sources in common, Figure 3 shows the comparison between the SFR values derived here and the ones obtained by PC13. As expected, PC13 SFR results agree better with the MIPS SFR, since they also obtained their SFR from the total $L_{\rm IR}$, which in turn was obtained by fitting the same SED templates used here, although we can notice some systematic offset of PC13 SFR values being lower than MIPS SFR, specially for SFR $< 5 M_\odot$ Sun/year. As mentioned before, PC13 used a shallower data set and the methods to measure the flux density were different. Thus, the faintest sources are the ones with greater differences in SFR determination between our method and PC13.

We now analyze how the SFR and the SSFR of our galaxies depend on environment. Here, it is important to highlight that we often find in the literature two different proxies for environment: the cluster centric radius and the local galaxy density, which is calculated from the distance to the 10th nearest neighbor (e.g., Noble et al. 2013). The former, which is used in this work, is a better indicator of the global environment and cluster potential. Although the local density has a proximate effect on galaxies, the cluster has been in existence about 2.5 Gyr. Thus, the current location may not be a good indicator of the galaxy's average local environment. We note that our radial measurements do not require a completeness correction since the completeness bias for mass is similar at all radii.

To analyze our correlations, we applied a robust linear regression fit and a Pearson linear correlation coefficient, which we list in Table 2. In the left panel of Figure 4, we plot the SFR of each of our cluster galaxies as a function of its projected cluster centric distance (our proxy for the cluster environment), for the SFR derived from MIPS observations (left panel) and using the MAGPHYS code (right panel). The black solid lines represent the best fit for the whole sample. The different symbols represent galaxies of different stellar masses. Black solid points
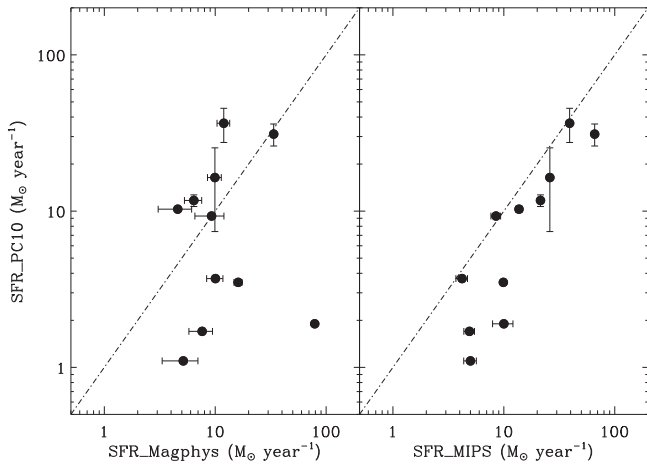
Figure 3. Comparison of the 11 sources we have in common with Pintos-Castro et al. (2013). We present a comparison of their SFR values against the one presented here determined using MAGPHYS code (left panel) and MIPS (right panel). The dotted–dashed lines represent the one-to-one correspondence.

represent less massive galaxies with $M_\star < 1.2 \times 10^{11} M_\odot$ (the median value of our sample) and the black dotted line represents the best fit for these galaxies. The red open triangles represent the most massive galaxies with masses $M_\star \geqslant 1.2 \times 10^{11} M_\odot$, and the red dotted line represents the best fit for these more massive galaxies. The plot that correspond to MAGPHYS SFRs shows that the SFR decreases with projected distance, in which galaxies at the center have higher SFR. For the $\mathrm{SFR_{MIPS}}$–Distance relation, if we look at distances larger than 0.2 Mpc, where most galaxies are, it is hard to see a dependence of the SFR on the projected distance. When we separate galaxies by mass, the SFR–Distance relation is steeper for more massive galaxies (with a linear Pearson correlation coefficient of −0.78) than for the less massive ones, in which SFR–Distance is consistent with no correlation. Here, we reinforce the fact that for higher mass galaxies the two innermost galaxies are driving the correlation. If we consider galaxies at distances larger than 0.2 Mpc, there is no correlation between SFR and Distance.

In the right panel of Figure 4, we plot the SFR as a function of the galaxy stellar mass for our galaxies. The black solid lines represent the best fit for the sample. The different symbols represent galaxies in different radii, where black solid points represent galaxies inside r_{500} and the black dotted line represents the best fit for these galaxies. The open red triangles represent galaxies outside r_{500}, and the red dotted line represents the best fit for these galaxies. For these panels, we see that the SFR–$M_\star$ relation presents a mild increase (with a Pearson correlation coefficient of about 0.20 for both methods). However, when we separate galaxies by distance, the SFR presents the same dependence on stellar mass for galaxies inside and outside r_{500} and both being consistent with no correlation. This indicates that the galaxies maintain almost the same SF at all densities (consistent with previous studies such as Peng et al. 2010; Lu et al. 2012; Muzzin et al. 2012).

We also show as a comparison two blue dotted–dashed lines in the right panels of Figure 4 that correspond to the main-sequence trend in the field at two different redshifts: 0.1 from the Sloan Digital Sky Survey (SDSS; Brinchmann et al. 2004) as analyzed by Elbaz et al. (2007) and the blue star-forming galaxies at $z = 0.8$–1.2 from the Great Observatories Origins Deep Survey (GOODS; Elbaz et al. 2007). These lines are important to guide our analysis. What can be seen from this figure is that the SFR of

most galaxies is closer to the main-sequence trend observed in the $z \sim 0$ SDSS field than to the main-sequence trend observed in the $z \sim 1$ GOODS field galaxies (although for MIPS SFRs there are $\sim 1/3$ close to $z \sim 1$). For the MAGPHYS SFRs, the few galaxies closer to the $z \sim 1$ trend are the less massive ones and there seems to be no preference of location in the cluster.

In principle, Figure 4 suggests that SFR is not related to the environment (traced by the cluster centric distance), but to galaxy mass. However, when trying to understand the role of environment on galaxy activity, one has to be aware that the most massive galaxies are located preferentially in denser environments. It is therefore difficult to separate the effect of external conditions from the increased in situ activity due to a larger galaxy mass. Thus, in hopes of identifying if more massive galaxies have indeed enhanced SFR, we have plotted in Figure 5 the SSFR against the projected cluster centric distance and stellar mass.

As we can see from the left panel of Figure 5, there is no dependence of the SSFR with cluster distance, but the SSFR is decreasing with stellar mass (Pearson correlation coefficient of −0.75), meaning that more massive galaxies are forming fewer stars per unit of mass, and most likely these are the galaxies that will populate the red sequence of clusters. This is consistent with the evolution of the mass function (e.g., Kodama et al. 2004), which shows that the massive end of galaxy mass function in cluster is in place by $z \sim 1$ and the evolution between $z = 0$–1 consists of a build-up of the $\leqslant 10^{11} M_\odot$ end. We also show in this figure that the bulk of SF has not yet taken place for approximately half of the galaxies, since most of them lie above the dotted–dashed line that indicates the SSFR at which the stellar mass doubles by at $z = 0$ if the SFR remains constant (Patel et al. 2009).

5. DISCUSSION

We have analyzed a single $z = 0.866$ young galaxy cluster from multi-wavelength perspective, and we investigated the dependence of SF activity as a function of cluster centric distance (a proxy for environment density) and stellar mass for 18 spectroscopically confirmed members. We computed the SFRs using two independent methods: extrapolating the observed 24 μm emission to get the total infrared luminosity, and modeling the full SEDs with the MAGPHYS code.

Our work allows us to assess the role of the environment and stellar mass on SFRs and we find that MIPS cluster members share certain properties with field galaxies, presenting a SFR that follows $z \sim 0$ field galaxies, and most of them populate the outskirts of the cluster. In fact, a non-negligible fraction of cluster members are forming stars actively.

If the SFRs are higher for more massive galaxies, when we investigate the SSFRs as a function of stellar mass, we find out that it is the less massive galaxies that are forming the bulk of stars. If the environment is somehow driving the SF, one would expect a relation between the SSFR and the cluster centric distance, but that is not the case. This result offers a hint at an alternative interpretation, as suggested by Noble et al. (2013): it indicates that inner regions of the cluster are not only populated by galaxies that has already spent a great time in in dense environments, but it is also polluted by infalling high-velocity galaxies that could be on their pass through the cluster center and are therefore not virialized with the core population. This can be seen by the black filled circles in Figure 6 that present velocity dispersion of about 600 km s^{-1} (and a galaxy near the cluster center with absolute line of sight velocity of almost of 2000 km s^{-1}). As these systems have
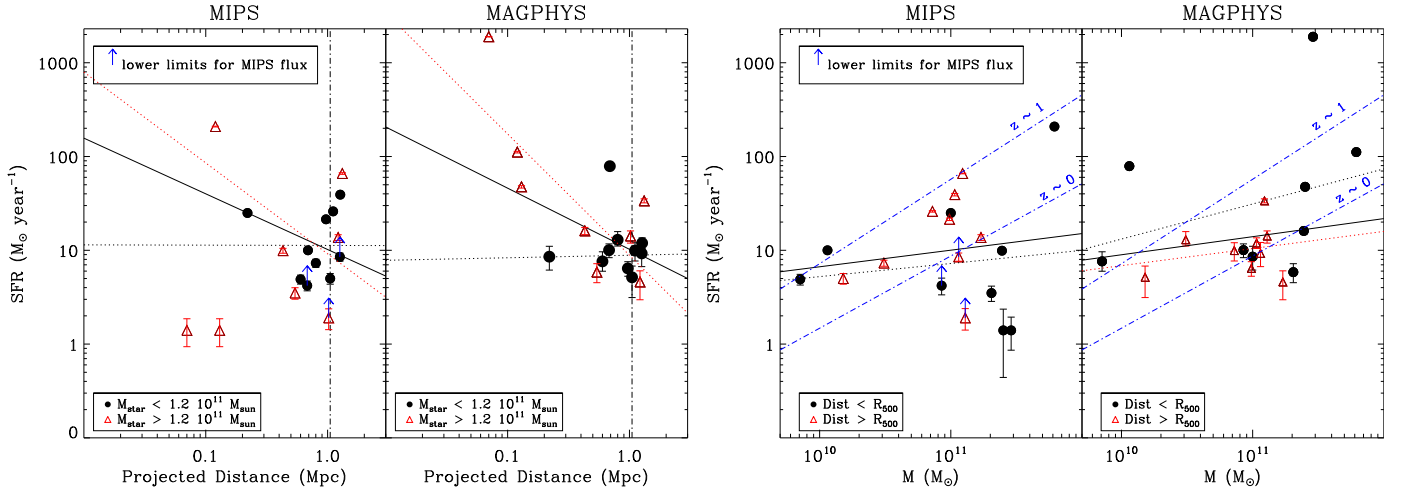
Figure 4. SFRs as a function of the projected distance from the center (left panels) and stellar masses (right panels) for SFRs computed from MIPS and using MAGPHYS code. In panels in which the SFR was computed from MIPS flux, we overplot blue upward arrows for the sources for which we used reduced apertures to get the flux due to nearby sources. The solid black lines correspond to the best fit for the whole sample. The red dotted lines represent the best fit for the red points, and the black dotted lines are the best fit for the black points. In the left panels, the black filed circles represent less massive galaxies with stellar masses $M_\star < 1.2 \times 10^{11} M_\odot$, and the open red triangles represent more massive galaxies, with $M_\star > 1.2 \times 10^{11} M_\odot$. In the right panels, the black filed circles represent the galaxies within r_{500} ($\sim$2/3 viral radius) and the open red triangles represent galaxies outside r_{500}. The dotted–dashed blue lines correspond to the field trend at $z = 0, 1$, respectively.
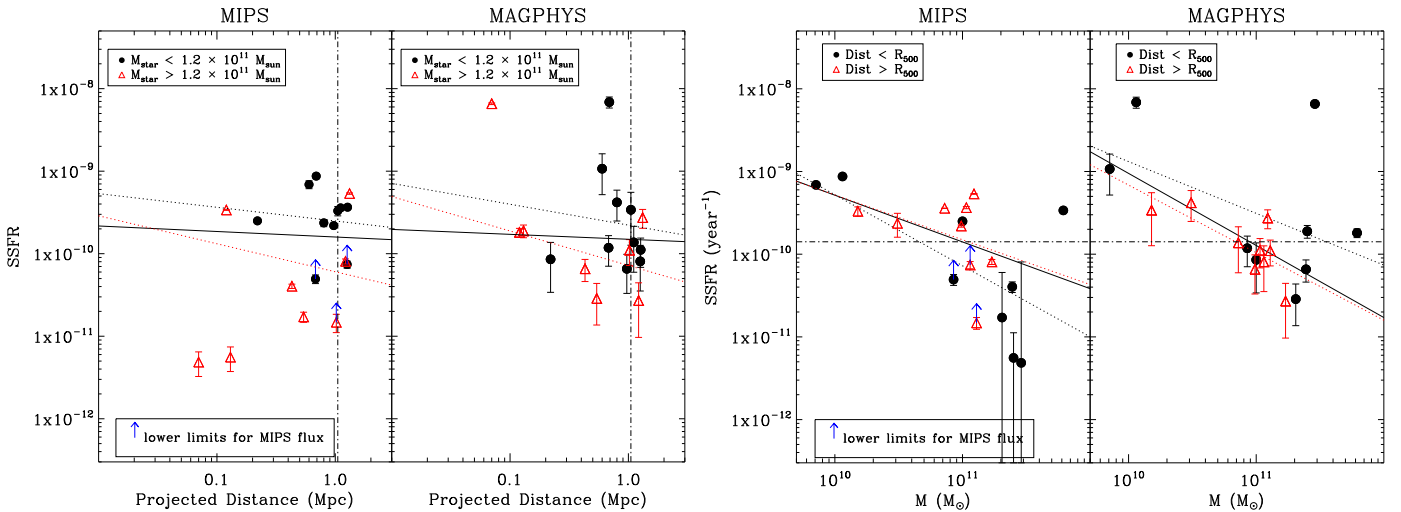

Figure 5. SSFRs as a function of projected distance from the center (left panel) and stellar mass (right panel). The symbols follow those in Figure 4. The dotted–dashed horizontal line in the right panels represents the SSFR at which stellar mass doubles by at $z = 0$ if the SFR remains the same (Patel et al. 2009).

retained a nominal level of SF for their stellar mass, they enhance the average SSFR in the inner radial bin (cluster core).

As already reported in Ulmer et al. (2009), this cluster is currently in the process of formation, presenting a bimodal distribution of X-ray emission, the presence of substructures and a high kT compared to the $L_{X, bol}-kT$ relation. This process of build up can explain most of the results found here. A non-negligible fraction of cluster members are forming stars actively, and that infall is probably responsible for much of the SF activity we see in the cluster. It is unlikely that a cluster only passively accretes star-forming galaxies from the surrounding field, and those galaxies have a higher level of SF simply because they were field galaxies. On the contrary, since we analyzed these relations as a function of the cluster centric distance that is a tracer of the global environment and potential well, it is possible that we are seeing an increased

SFR in infalling galaxies triggered by the galaxy–IGM interaction as shown by previous theoretical and observational evidence (e.g., Gavazzi et al. 1995; Bai et al. 2007).

6. CONCLUSIONS

Our work highlights the significant role of the environment in the SF activity of the young cluster RX J1257+4738. We use the deepest existing mid-infrared survey at 24 μm, with some of the largest spectroscopic completeness to analyze the relationship between the SFR and SSFR as a function of projected cluster centric distance (as a proxy of the density) in a galaxy cluster at $z \sim 0.9$. In summary, our analysis lead to the following conclusions.

1. We showed that when we separate galaxies by mass, more massive galaxies tend to have a higher SFR than less massive ones. However, the SFR–$M_\star$ relation is
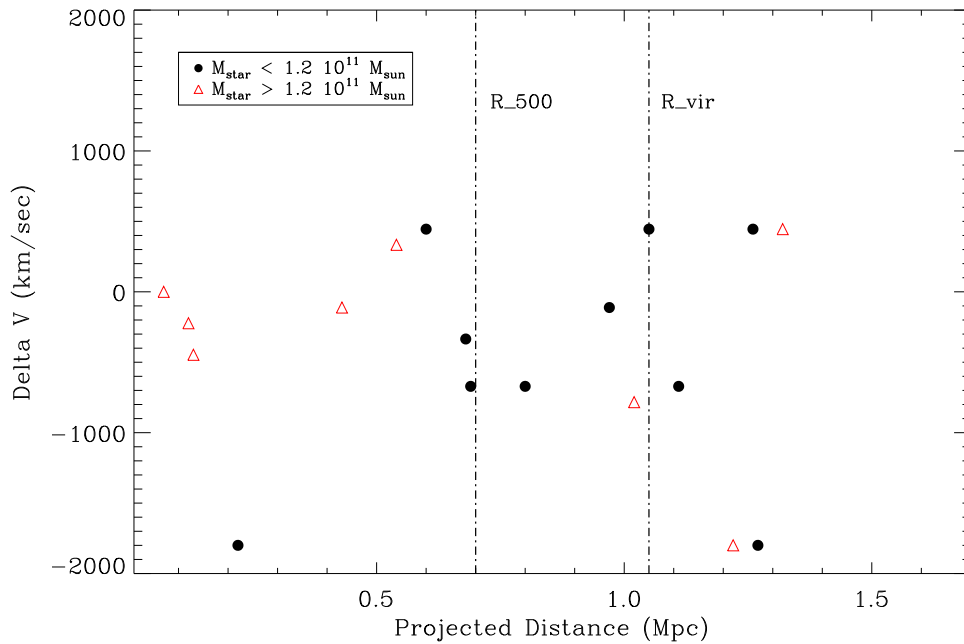
Figure 6. Absolute line of sight velocity as a function of projected radius. The two vertical dotted–dashed lines correspond to r_{500} and r_{vir} and the different symbols represent galaxies of different mass with color identification as the left panels of Figures 4 and 5.

independent of the projected cluster centric radius, indicating that galaxies display almost the same SF at all densities. In principle, these results indicate that SFR is not related to environment but to stellar mass.

2. In order to understand whether the SFR–density relation is generated by the presence of the massive galaxies in denser regions, we showed that the SSFR slowly decreases with stellar mass, showing that the less massive galaxies are forming the bulk of stars. This indicates that the increase in SF is driven by cluster assembly and galaxy infall. If environment is driving SF, one would expect a relation between the SSFR and the projected distance, that is not observed in our data.

3. A possible scenario to explain this lack of correlation is the contamination by high-velocity galaxies in the inner part of the cluster which could be infalling galaxies that may be on their initial pass through the cluster center and therefore are still not virialized with the core population. As these systems have retained a nominal level of SF for their stellar mass, they enhance the mean SSFR in the center (inside r_{500}).

APPENDIX A
NOTES ON INDIVIDUAL GALAXIES

Here we give more details about the sources that we used a reduced aperture to get MIPS flux density and also a merging pair of galaxy that might have the total flux contaminated.

1. Sources 1, 6, and 17: These source have a I1 –FluxType=4, which means that this source is real but its flux density cannot be measured accurately and we had to use a reduced aperture (due to nearby sources) to get the flux density and the values presented in Table 1 are lower limit values. Sources 1 and 6: These sources are clearly about 10 sigma by eye, but there are several sources nearby so that we used a 2.5 pixel radius aperture. The uncertainties are based on the SHA provided values elsewhere and that the uncertainty map is nearly constant for the inner region. Source 17: This source is only 3.4 SNR in SHA table, thus we used reduced aperture to get flux due to nearby source. Instead of fixed MISP aperture of 7.35 pixels, we used 4 pixels.

2. Source 10 (R.A. decl.): This is a clearly merging pair of galaxies. The total flux obtained from MIPS might not be due to a single galaxy.

APPENDIX B
BEST FITS

8

Table 2
We Applied a Robust Linear Regression through Bisquare Weights Method to Obtain Power-law Fits, $\log(Y) = A + B \log(X)$

Y	X	Sample	A	B	Pearson Correlation Coef.
SFR_{MIPS}	Proj. Distance	Whole	0.95 ± 0.27	-0.59 ± 0.21	-0.34
SFR_{MIPS}	Proj. Distance	$M_\star \leqslant 1.2 \times 10^{11} M_\odot$	1.03 ± 0.17	-0.0030 ± 0.19	-0.0038
SFR_{MIPS}	Proj. Distance	$M_\star \geqslant 1.2 \times 10^{11} M_\odot$	0.96 ± 0.35	-0.97 ± 0.34	-0.49
$SFR_{MAGPHYS}$	Proj. Distance	Whole	1.01 ± 0.17	-0.65 ± 0.16	-0.53
$SFR_{MAGPHYS}$	Proj. Distance	$M_\star \leqslant 1.2 \times 10^{11} M_\odot$	0.95 ± 0.47	0.027 ± 0.35	-0.066
$SFR_{MAGPHYS}$	Proj. Distance	$M_\star \geqslant 1.2 \times 10^{11} M_\odot$	0.98 ± 0.47	-1.29 ± 0.13	-0.79
SFR_{MIPS}	$M_\star$	Whole	-0.95 ± 0.47	0.18 ± 0.13	0.17
SFR_{MIPS}	$M_\star$	Dist $\leqslant r_{500}$	-0.68 ± 0.21	0.14 ± 0.14	0.16
SFR_{MIPS}	$M_\star$	Dist $\geqslant r_{500}$	-3.87 ± 0.45	0.45 ± 0.19	0.31
$SFR_{MAGPHYS}$	$M_\star$	Whole	-0.97 ± 0.64	0.19 ± 0.10	0.22
$SFR_{MAGPHYS}$	$M_\star$	Dist $\leqslant r_{500}$	-0.41 ± 0.37	0.15 ± 0.18	0.20
$SFR_{MAGPHYS}$	$M_\star$	Dist $\geqslant r_{500}$	-0.99 ± 0.77	0.18 ± 0.16	0.23
$SSFR_{MIPS}$	Proj. Distance	Whole	-9.80 ± 0.26	-0.067 ± 0.09	-0.03
$SSFR_{MIPS}$	Proj. Distance	$M_\star \leqslant 1.2 \times 10^{11} M_\odot$	-9.60 ± 1.61	-0.16 ± 0.10	-0.10
$SSFR_{MIPS}$	Proj. Distance	$M_\star \geqslant 1.2 \times 10^{11} M_\odot$	-10.22 ± 0.63	-0.33 ± 0.13	-0.19
$SSFR_{MAGPHYS}$	Proj. Distance	Whole	-9.82 ± 1.82	-0.060 ± 0.26	-0.031
$SSFR_{MAGPHYS}$	Proj. Distance	$M_\star \leqslant 1.2 \times 10^{11} M_\odot$	-9.65 ± 2.92	-0.25 ± 0.12	-0.10
$SSFR_{MAGPHYS}$	Proj. Distance	$M_\star \geqslant 1.2 \times 10^{11} M_\odot$	-10.22 ± 0.27	-0.32 ± 0.11	-0.33
$SSFR_{MIPS}$	$M_\star$	Whole	-3.63 ± 0.80	-0.57 ± 0.24	-0.52
$SSFR_{MIPS}$	$M_\star$	Dist $\leqslant r_{500}$	-0.66 ± 0.21	-0.86 ± 0.36	-0.63
$SSFR_{MIPS}$	$M_\star$	Dist $\geqslant r_{500}$	-3.87 ± 1.51	-0.54 ± 0.35	-0.39
$SSFR_{MAGPHYS}$	$M_\star$	Whole	-0.31 ± 0.16	-0.87 ± 0.18	-0.75
$SSFR_{MAGPHYS}$	$M_\star$	Dist $\leqslant r_{500}$	-2.62 ± 1.06	-0.62 ± 0.30	-0.46
$SSFR_{MAGPHYS}$	$M_\star$	Dist $\geqslant r_{500}$	-0.99 ± 0.17	-0.81 ± 0.26	-0.74

Note. Uncertainties were determined using a bootstrap linear fit to the data with 100 resampling.
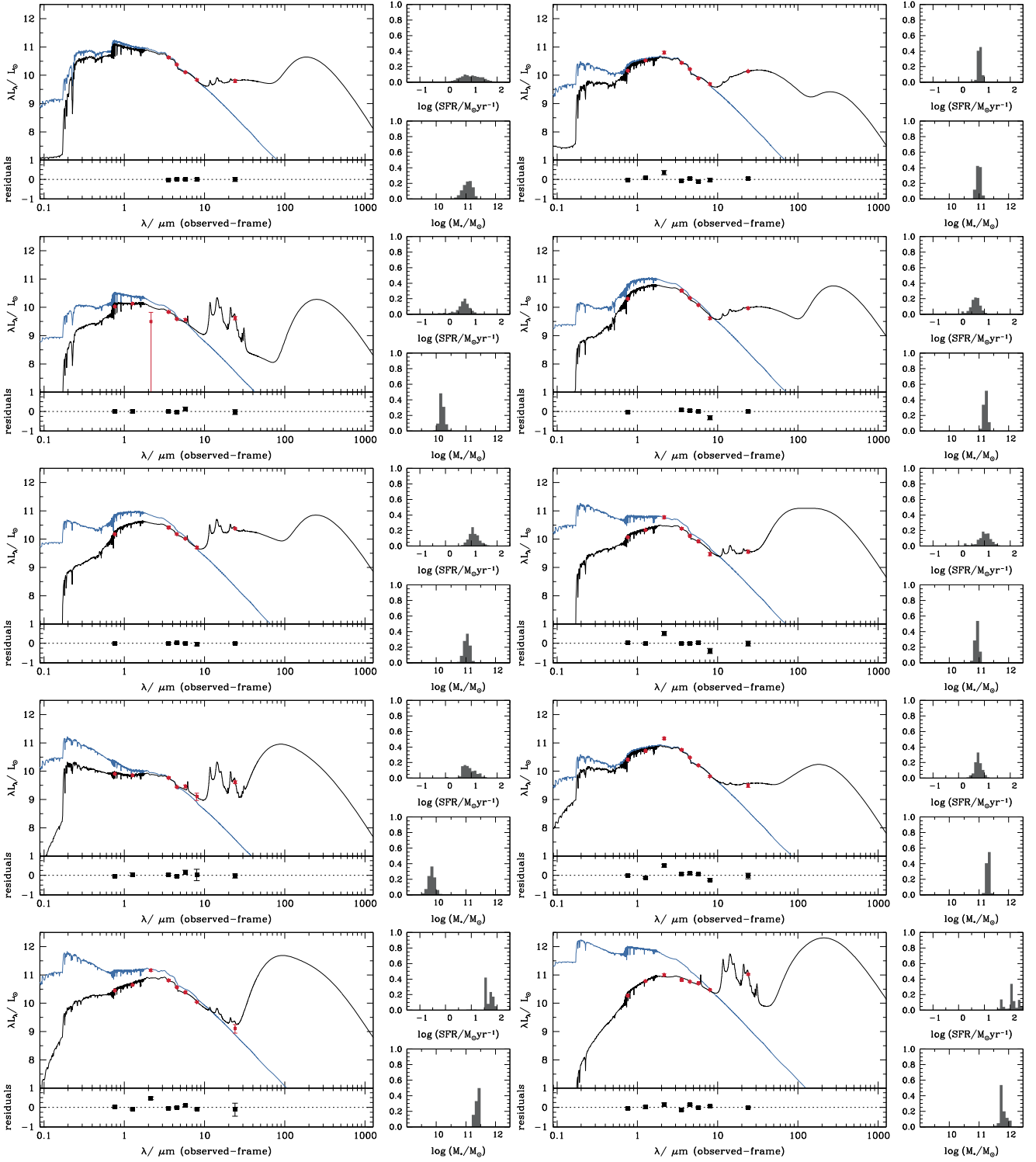
APPENDIX C
MAGPHYS PLOTS

Figure 7. Best model fits (black line) to the observed spectral energy distribution (red points) of the galaxies. In each panel, the blue line is the unattenuated stellar population spectrum. For each observational point, the vertical error bar indicates the measurement error. The two minor panels show the likelihood distribution of SFR (upper right panel) and stellar mass (lower right panel) derived from fits to the observed spectral energy distribution. From top to bottom and left to right, galaxies are in R.A. order, as presented in Table 1, with source codes: 1, 2, 3, 4, 5, 6, 7, 8, 9, and 10.
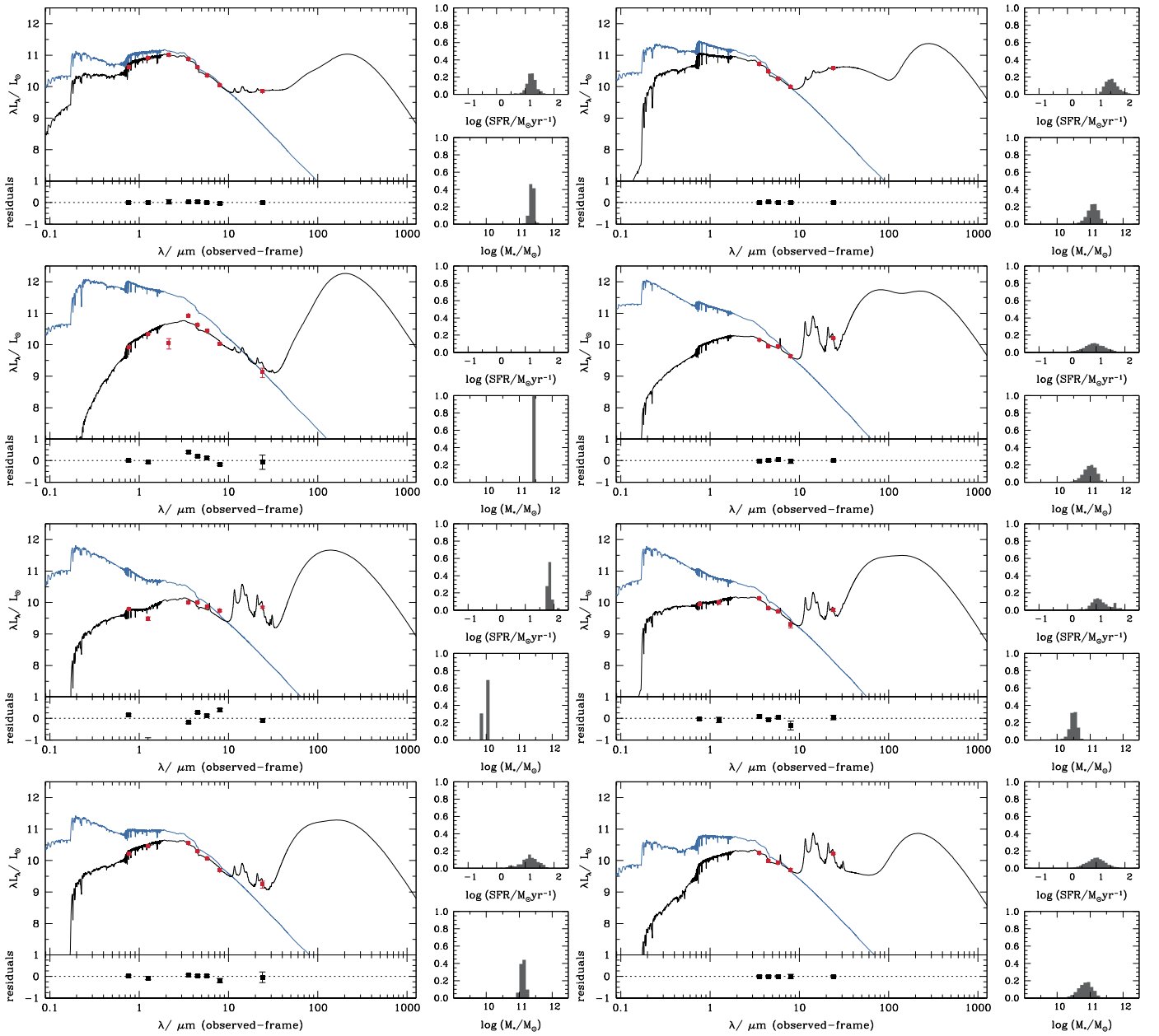
Figure 8. Best model fits (black line) to the observed spectral energy distribution (red points) of the galaxies. In each panel, the blue line shows the unattenuated stellar population spectrum. For each observational point, the vertical error bar indicates the measurement error. The two minor panels show the likelihood distribution of SFR (upper right panel) and stellar mass (lower right panel) derived from fits to the observed spectral energy distribution. From top to bottom and left to right, galaxies are in R.A. order, as presented in Table 1, with source codes: 11, 12, 13, 14, 15, 16, 17, and 18.

REFERENCES

Bai, L., Marcillac, D., Rieke, G. H., et al. 2007, ApJ, 664, 181
Balogh, M., Eke, V., Miller, C., et al. 2004, MNRAS, 348, 1355
Blanton, M. R., & Moustakas, J. 2009, ARA&A, 47, 159
Brinchmann, J., Charlot, S., White, S. D. M., et al. 2004, MNRAS, 351, 1151
Bruzual, G., & Charlot, S. 2003, MNRAS, 344, 1000
Butcher, H., & Oemler, A., Jr. 1978, ApJ, 219, 18
Calzetti, D., Wu, S.-Y., Hong, S., et al. 2010, ApJ, 714, 1256
Chabrier, G. 2003, PASP, 115, 763
Charlot, S., & Fall, S. M. 2000, ApJ, 539, 718
Chary, R., & Elbaz, D. 2001, ApJ, 556, 562
Cooper, M. C., Newman, J. A., Croton, D. J., et al. 2006, MNRAS, 370, 198
Cooper, M. C., Newman, J. A., Weiner, B. J., et al. 2008, MNRAS, 383, 1058
Cucciati, O., Iovino, A., Marinoni, C., et al. 2006, A&A, 458, 39
da Cunha, E., Charlot, S., & Elbaz, D. 2008, MNRAS, 388, 1595
Donley, J. L., Koekemoer, A. M., Brusa, M., et al. 2012, ApJ, 748, 142

Dressler, A. 1980, ApJ, 236, 351
Elbaz, D., Daddi, E., Le Borgne, D., et al. 2007, A&A, 468, 33
Engelbracht, C. W., Gordon, K. D., Rieke, G. H., et al. 2005, ApJL, 628, L29
Fazio, G. G., Hora, J. L., Allen, L. E., et al. 2004, ApJS, 154, 10
Gavazzi, G., Randone, I., & Branchini, E. 1995, ApJ, 438, 590
Genzel, R., Tacconi, L. J., Gracia-Carpio, J., et al. 2010, MNRAS, 407, 2091
Giard, M., Lamarre, J. M., Pajot, F., & Serra, G. 1994, A&A, 286, 203
Gómez, P. L., Nichol, R. C., Miller, C. J., et al. 2003, ApJ, 584, 210
Hilton, M., Collins, C. A., Stanford, S. A., et al. 2007, ApJ, 670, 1000
Hopkins, A. M., & Beacom, J. F. 2006, ApJ, 651, 142
Kauffmann, G., White, S. D. M., Heckman, T. M., et al. 2004, MNRAS, 353, 713
Kennicutt, R. C., Jr. 1998, ARA&A, 36, 189
Kodama, T., Yamada, T., Akiyama, M., et al. 2004, MNRAS, 350, 1005
Kravtsov, A. V., & Borgani, S. 2012, ARA&A, 50, 353
Lacy, M., Petric, A. O., Sajina, A., et al. 2007, AJ, 133, 186
Le Floc'h, E., Papovich, C., Dole, H., et al. 2005, ApJ, 632, 169

Lilly, S. J., Le Fevre, O., Hammer, F., & Crampton, D. 1996, ApJL, 460, L1

Lu, T., Gilbank, D. G., McGee, S. L., Balogh, M. L., & Gallagher, S. 2012, MNRAS, 420, 126

Madau, P., Ferguson, H. C., Dickinson, M. E., et al. 1996, MNRAS, 283, 1388

Madden, S. C., Galliano, F., Jones, A. P., & Sauvage, M. 2006, A&A, 446, 877

Muzzin, A., Wilson, G., Yee, H. K. C., et al. 2012, ApJ, 746, 188

Noble, A. G., Webb, T. M. A., Muzzin, A., et al. 2013, ApJ, 768, 118

Patel, S. G., Holden, B. P., Kelson, D. D., Illingworth, G. D., & Franx, M. 2009, ApJL, 705, L67

Patel, S. G., Kelson, D. D., Holden, B. P., Franx, M., & Illingworth, G. D. 2011, ApJ, 735, 53

Peng, Y.-j., Lilly, S. J., Kovač, K., et al. 2010, ApJ, 721, 193

Pintos-Castro, I., Sánchez-Portal, M., Cepa, J., et al. 2013, A&A, 558, A100

Rieke, G. H., Young, E. T., Engelbracht, C. W., et al. 2004, ApJS, 154, 25

Saintonge, A., Tran, K.-V. H., & Holden, B. P. 2008, ApJL, 685, L113

Salpeter, E. E. 1955, ApJ, 121, 161

Stern, D., Eisenhardt, P., Gorjian, V., et al. 2005, ApJ, 631, 163

Stetson, P. B. 1987, PASP, 99, 191

Stetson, P. B. 1992, JRASC, 86, 71

Ulmer, M. P., Adami, C., Lima Neto, G. B., et al. 2009, A&A, 503, 399

Webb, T. M. A., O'Donnell, D., Yee, H. K. C., et al. 2013, AJ, 146, 84